

Visualizing the near-field coupling and interference of bonding and anti-bonding modes in infrared dimer nanoantennas

Pablo Alonso-González,^{1,*} Pablo Albella,² Federico Golmar,^{1,3} Libe Arzubiaga,¹ Félix Casanova,^{1,4} Luis E. Hueso,^{1,4} Javier Aizpurua,² and Rainer Hillenbrand^{1,4,5}

¹Nanooptics Group, CIC nanoGUNE Consolider, 20018 Donostia – San Sebastián, Spain
²Centro de Física de Materiales (CSIC-UPV/EHU) and Donostia International Physics Center (DIPC), 20018 Donostia-San Sebastián, Spain

³I.N.T.I.–CONICET, Av. Gral. Paz 5445, Ed. 42, B1650JKA, San Martín, Bs As, Argentina

⁴IKERBASQUE, Basque Foundation for Science, 48011 Bilbao, Spain

⁵r.hillenbrand@nanogune.eu

*palonso@nanogune.eu

Abstract: We directly visualize and identify the capacitive coupling of infrared dimer antennas in the near field by employing scattering-type scanning near-field optical microscopy (s-SNOM). The coupling is identified by (i) resolving the strongly enhanced nano-localized near fields in the antenna gap and by (ii) tracing the red shift of the dimer resonance when compared to the resonance of the single antenna constituents. Furthermore, by modifying the illumination geometry we break the symmetry, providing a means to excite both the bonding and the “dark” anti-bonding modes. By spectrally matching both modes, their interference yields an enhancement or suppression of the near fields at specific locations, which could be useful in nanoscale coherent control applications.

©2013 Optical Society of America

OCIS codes: (180.4243) Near-field microscopy; (110.3080) Infrared imaging; (250.5403) Plasmonics; (260.3910) Metal optics.

References and links

1. H. Xu, J. Aizpurua, M. Käll, and P. Apell, “Electromagnetic contributions to single-molecule sensitivity in surface-enhanced Raman scattering,” *Phys. Rev. E* **62**(3 Pt B), 4318–4324 (2000).
2. J. A. Schuller, E. S. Barnard, W. Cai, Y. C. Jun, J. S. White, and M. L. Brongersma, “Plasmonics for extreme light concentration and manipulation,” *Nat. Mater.* **9**(3), 193–204 (2010).
3. L. Novotny and N. van Hulst, “Antennas for light,” *Nat. Photonics* **5**(2), 83–90 (2011).
4. N. J. Halas, S. Lal, W.-S. Chang, S. Link, and P. Nordlander, “Plasmons in strongly coupled metallic nanostructures,” *Chem. Rev.* **111**(6), 3913–3961 (2011).
5. H. Xu, E. J. Bjerneld, M. Käll, and L. Börjesson, “Spectroscopy of single hemoglobin molecules by surface enhanced Raman scattering,” *Phys. Rev. Lett.* **83**(21), 4357–4360 (1999).
6. N. Liu, M. Hentschel, T. Weiss, A. P. Alivisatos, and H. Giessen, “Three-dimensional plasmon rulers,” *Science* **332**(6036), 1407–1410 (2011).
7. M. W. Knight, H. Sobhani, P. Nordlander, and N. J. Halas, “Photodetection with active optical antennas,” *Science* **332**(6030), 702–704 (2011).
8. C. Radloff and N. J. Halas, “Plasmonic properties of concentric nanoshells,” *Nano Lett.* **4**(7), 1323–1327 (2004).
9. A. G. Curto, G. Volpe, T. H. Taminiau, M. P. Kreuzer, R. Quidant, and N. F. van Hulst, “Unidirectional emission of a quantum dot coupled to a nanoantenna,” *Science* **329**(5994), 930–933 (2010).
10. J. Pérez-Juste, I. Pastoriza-Santos, L. M. Liz-Marzán, and P. Mulvaney, “Gold nanorods: synthesis, characterization and applications,” *Coord. Chem. Rev.* **249**(17-18), 1870–1901 (2005).
11. L. Chuntonov and G. Haran, “Trimeric plasmonic molecules: the role of symmetry,” *Nano Lett.* **11**(6), 2440–2445 (2011).
12. M. Hentschel, M. Saliba, R. Vogelgesang, H. Giessen, A. P. Alivisatos, and N. Liu, “Transition from isolated to collective modes in plasmonic oligomers,” *Nano Lett.* **10**(7), 2721–2726 (2010).
13. N. Verellen, P. Van Dorpe, C. Huang, K. Lodewijks, G. A. E. Vandenbosch, L. Lagae, and V. V. Moshchalkov, “Plasmon line shaping using nanocrosses for high sensitivity localized surface plasmon resonance sensing,” *Nano Lett.* **11**(2), 391–397 (2011).
14. V. Giannini, A. I. Fernández-Domínguez, S. C. Heck, and S. A. Maier, “Plasmonic nanoantennas: fundamentals and their use in controlling the radiative properties of nanoemitters,” *Chem. Rev.* **111**(6), 3888–3912 (2011).

15. W. Rechberger, A. Hohenau, A. Leitner, J. R. Krenn, B. Lamprecht, and F. R. Aussenegg, "Optical properties of two interacting gold nanoparticles," *Opt. Commun.* **220**(1-3), 137–141 (2003).
16. P. Ghenuche, S. Cherukulappurath, T. H. Taminiau, N. F. van Hulst, and R. Quidant, "Spectroscopic mode mapping of resonant plasmon nanoantennas," *Phys. Rev. Lett.* **101**(11), 116805 (2008).
17. P. Mühlischlegel, H. J. Eisler, O. J. F. Martin, B. Hecht, and D. W. Pohl, "Resonant optical antennas," *Science* **308**(5728), 1607–1609 (2005).
18. M. Schnell, A. Garcia-Etxarri, J. Alkorta, J. Aizpurua, and R. Hillenbrand, "Phase-resolved mapping of the near-field vector and polarization state in nanoscale antenna gaps," *Nano Lett.* **10**(9), 3524–3528 (2010).
19. I. Alber, W. Sigle, S. Müller, R. Neumann, O. Picht, M. Rauber, P. A. van Aken, and M. E. Toimil-Molares, "Visualization of multipolar longitudinal and transversal surface plasmon modes in nanowire dimers," *ACS Nano* **5**(12), 9845–9853 (2011).
20. J. Dorfmueller, D. Dregely, M. Esslinger, W. Khunsin, R. Vogelgesang, K. Kern, and H. Giessen, "Near-field dynamics of optical Yagi-Uda nanoantennas," *Nano Lett.* **11**(7), 2819–2824 (2011).
21. D. P. Fromm, A. Sundaramurthy, P. J. Schuck, G. Kino, and W. E. Moerner, "Gap-dependent optical coupling of single "Bowtie" nanoantennas resonant in the visible," *Nano Lett.* **4**(5), 957–961 (2004).
22. T. G. Habteyes, S. Dhuey, S. Cabrini, P. J. Schuck, and S. R. Leone, "Theta-shaped plasmonic nanostructures: bringing "dark" multipole plasmon resonances into action via conductive coupling," *Nano Lett.* **11**(4), 1819–1825 (2011).
23. J.-S. Huang, J. Kern, P. Geisler, P. Weinmann, M. Kamp, A. Forchel, P. Biagioni, and B. Hecht, "Mode imaging and selection in strongly coupled nanoantennas," *Nano Lett.* **10**(6), 2105–2110 (2010).
24. D.-S. Kim, J. Heo, S.-H. Ahn, S. W. Han, W. S. Yun, and Z. H. Kim, "Real-space mapping of the strongly coupled plasmons of nanoparticle dimers," *Nano Lett.* **9**(10), 3619–3625 (2009).
25. R. L. Olmon, M. Rang, P. M. Krenz, B. A. Lail, L. V. Saraf, G. D. Boreman, and M. B. Raschke, "Determination of electric-field, magnetic-field, and electric-current distributions of infrared optical antennas: a near-field optical vector network analyzer," *Phys. Rev. Lett.* **105**(16), 167403 (2010).
26. M. Schnell, A. Garcia Etxarri, A. J. Huber, K. B. Crozier, J. Aizpurua, and R. Hillenbrand, "Controlling the near-field oscillations of loaded plasmonic nanoantennas," *Nat. Photonics* **3**(5), 287–291 (2009).
27. L. Shao, K. C. Woo, H. Chen, Z. Jin, J. Wang, and H.-Q. Lin, "Angle- and energy-resolved plasmon coupling in gold nanorod dimers," *ACS Nano* **4**(6), 3053–3062 (2010).
28. T. Shegai, S. Chen, V. D. Miljkovic, G. Zengin, P. Johansson, and M. Kall, "A bimetallic nanoantenna for directional colour routing," *Nat. Communications* **2**(481), 1–6 (2011).
29. L. S. Slaughter, Y. Wu, B. A. Willingham, P. Nordlander, and S. Link, "Effects of symmetry breaking and conductive contact on the plasmon coupling in gold nanorod dimers," *ACS Nano* **4**(8), 4657–4666 (2010).
30. A. M. Funston, C. Novo, T. J. Davis, and P. Mulvaney, "Plasmon coupling of gold nanorods at short distances and in different geometries," *Nano Lett.* **9**(4), 1651–1658 (2009).
31. T. J. Davis, D. E. Gómez, and K. C. Vernon, "Simple model for the hybridization of surface plasmon resonances in metallic nanoparticles," *Nano Lett.* **10**(7), 2618–2625 (2010).
32. E. Prodan, C. Radloff, N. J. Halas, and P. Nordlander, "A hybridization model for the plasmon response of complex nanostructures," *Science* **302**(5644), 419–422 (2003).
33. P. Alonso-Gonzalez, M. Schnell, P. Sarriugarte, H. Sobhani, C. Wu, N. Arju, A. Khanikaev, F. Golmar, P. Albella, L. Arzubiaga, F. Casanova, L. E. Hueso, P. Nordlander, G. Shvets, and R. Hillenbrand, "Real-space mapping of Fano interference in plasmonic metamolecules," *Nano Lett.* **11**(9), 3922–3926 (2011).
34. J. A. Fan, K. Bao, C. Wu, J. Bao, R. Bardhan, N. J. Halas, V. N. Manoharan, G. Shvets, P. Nordlander, and F. Capasso, "Fano-like interference in self-assembled plasmonic quadrumer clusters," *Nano Lett.* **10**(11), 4680–4685 (2010).
35. J. A. Fan, C. Wu, K. Bao, J. Bao, R. Bardhan, N. J. Halas, V. N. Manoharan, P. Nordlander, G. Shvets, and F. Capasso, "Self-assembled plasmonic nanoparticle clusters," *Science* **328**(5982), 1135–1138 (2010).
36. A. E. Miroshnichenko, S. Flach, and Y. S. Kivshar, "Fano resonances in nanoscale structures," *Rev. Mod. Phys.* **82**(3), 2257–2298 (2010).
37. N. Verellen, Y. Sonnefraud, H. Sobhani, F. Hao, V. V. Moshchalkov, P. Van Dorpe, P. Nordlander, and S. A. Maier, "Fano resonances in individual coherent plasmonic nanocavities," *Nano Lett.* **9**(4), 1663–1667 (2009).
38. M. Rahmani, B. Luk'yanchuk, and M. Hong, "Fano resonance in novel plasmonic nanostructures," *Laser & Photon. Rev.* doi: 10.1002/lpor.201200021 (2012).
39. N. Liu, T. Weiss, M. Mesch, L. Langguth, U. Eigenthaler, M. Hirscher, C. Sönnichsen, and H. Giessen, "Planar metamaterial analogue of electromagnetically induced transparency for plasmonic sensing," *Nano Lett.* **10**(4), 1103–1107 (2010).
40. N. Papasimakis, V. A. Fedotov, N. I. Zheludev, and S. L. Prosvirnin, "Metamaterial analog of electromagnetically induced transparency," *Phys. Rev. Lett.* **101**(25), 253903 (2008).
41. S. Zhang, D. A. Genov, Y. Wang, M. Liu, and X. Zhang, "Plasmon-induced transparency in metamaterials," *Phys. Rev. Lett.* **101**(4), 047401 (2008).
42. M. Rahmani, B. Lukiyanchuk, T. Tahmasebi, Y. Lin, T. Y. F. Liew, and M. H. Hong, "Polarization-controlled spatial localization of near-field energy in planar symmetric coupled oligomers," *Appl. Phys., A Mater. Sci. Process.* **107**(1), 23–30 (2012).
43. C. Wu, A. B. Khanikaev, R. Adato, N. Arju, A. A. Yanik, H. Altug, and G. Shvets, "Fano-resonant asymmetric metamaterials for ultrasensitive spectroscopy and identification of molecular monolayers," *Nat. Mater.* **11**(1), 69–75 (2011).
44. S. Mukherjee, H. Sobhani, J. B. Lassiter, R. Bardhan, P. Nordlander, and N. J. Halas, "Fanoshells: nanoparticles with built-in Fano resonances," *Nano Lett.* **10**(7), 2694–2701 (2010).

45. J. Aizpurua, G. W. Bryant, L. J. Richter, F. J. García de Abajo, B. K. Kelley, and T. Mallouk, "Optical properties of coupled metallic nanorods for field-enhanced spectroscopy," *Phys. Rev. B* **71**(235420), 1–13 (2005).
46. S. Mastel, S. E. Grefe, G. B. Cross, A. Taber, S. Dhuey, S. Cabrini, P. J. Schuck, and Y. Abate, "Real-space mapping of nanoplasmonic hotspots via optical antenna-gap loading," *Appl. Phys. Lett.* **101**(131102), 1–4 (2012).
47. G. Volpe, S. Cherukulappurath, R. Juanola Parramon, G. Molina-Terriza, and R. Quidant, "Controlling the optical near field of nanoantennas with spatial phase-shaped beams," *Nano Lett.* **9**(10), 3608–3611 (2009).
48. J. Chen, P. Albella, Z. Pirzadeh, P. Alonso-González, F. Huth, S. Bonetti, V. Bonanni, J. Åkerman, J. Nogués, P. Vavassori, A. Dmitriev, J. Aizpurua, and R. Hillenbrand, "Plasmonic nickel nanoantennas," *Small* **7**(16), 2341–2347 (2011).
49. P. Alonso-González, P. Albella, M. Schnell, J. Chen, F. Huth, A. García-Etxarri, F. Casanova, F. Golmar, L. Arzubiaga, L. E. Hueso, J. Aizpurua, and R. Hillenbrand, "Resolving the electromagnetic mechanism of surface-enhanced light scattering at single hot spots," *Nat. Communications* **3**(684), 1–7 (2012).
50. N. Ocelic, A. Huber, and R. Hillenbrand, "Pseudoheterodyne detection for background-free near-field spectroscopy," *Appl. Phys. Lett.* **89**(101124), 1–3 (2006).
51. P. Biagioni, M. Savoini, J.-S. Huang, L. Dúo, M. Finazzi, and B. Hecht, "Near-field polarization shaping by a near-resonant plasmonic cross antenna," *Phys. Rev. B* **80**(153409), 1–4 (2009).
52. Z.-G. Dong, H. Liu, M.-X. Xu, T. Li, S.-M. Wang, J.-X. Cao, S.-N. Zhu, and X. Zhang, "Role of asymmetric environment on the dark mode excitation in metamaterial analogue of electromagnetically-induced transparency," *Opt. Express* **18**(21), 22412–22417 (2010).
53. F. Neubrech, A. García-Etxarri, D. Weber, J. Bochterle, H. Shen, M. L. de la Chapelle, G. W. Bryant, J. Aizpurua, and A. Pucci, "Defect-induced activation of symmetry forbidden infrared resonances in individual metallic nanorods," *Appl. Phys. Lett.* **96**(213111), 1–3 (2010).
54. A. L. Koh, A. I. Fernández-Domínguez, D. W. McComb, S. A. Maier, and J. K. W. Yang, "High-resolution mapping of electron-beam-excited plasmon modes in lithographically defined gold nanostructures," *Nano Lett.* **11**(3), 1323–1330 (2011).

1. Introduction

Light illuminating a metal nanostructure can resonantly excite surface plasmons, which are collective oscillations of free electrons in the metal that lead to the formation of highly enhanced nano-localized optical fields at the metal surface, the so-called "hot spots" [1]. The frequency and intensity of these oscillations are highly sensitive to the nanostructure shape, size, and environment, offering the possibility to control and manipulate electromagnetic fields at the nanometer scale [2–4]. In the last years, this function of metal nanostructures has promoted the development of a large variety of applications including surface-enhanced Raman scattering (SERS) [5], nanoscale plasmon rulers [6], or novel enhanced photo-detection and photo-emission mechanisms [7].

A vast range of plasmonic antenna structures showing different functionalities have been proposed [8–14]. Particularly interesting are those formed by combinations of simple metallic elements that couple through near-field interaction [15–30] (often referred to as plasmonic molecules). Due to their coupling behavior, plasmonic molecules show the appearance of unique hybridized plasmon modes [23, 24, 29, 31, 32], in analogy to the hybridization of wave functions in molecules. Importantly, the near-field coupling of these modes in a plasmonic structure promotes the appearance of prominent interfering effects such as plasmonic Fano resonances [13, 33–38] or electromagnetic induced transparency (EIT) [39–41], which offer extended possibilities in the design and tuning of the antenna's optical response [4].

Although the study of coupling, hybridization and interference of plasmon modes has become increasingly ubiquitous in the literature during the last years, it has been mainly conducted by far-field characterization techniques on complex plasmonic structures such as oligomers [35, 42], "dolmen, Pi" antennas [43] or multilayer nanoshells [44], supported by near-field calculations. The ability to visualize and, more importantly, to tune these coupling phenomena in the near field of the plasmonic antennas will facilitate the creation and development of a variety of novel plasmonic devices, where the optical properties can be controlled at the nanoscale. One relevant example of a basic plasmonic structure showing coupling behavior is the dimer antenna, which is formed by two metal nanorods separated by a nanoscale gap [16, 17, 19, 23–26, 29, 30, 45, 46]. In such a dimer, the strong near-field interaction across the gap causes hybridization of plasmon modes that in analogy to the energy levels in a molecule leads to the splitting of modes into a lower-energy bonding mode

and a higher-energy anti-bonding mode. The bonding mode is characterized by a parallel alignment of the electric dipoles on each nanorod, producing strong field enhancement in the gap region. The anti-bonding mode is defined by an anti-parallel alignment of the dipoles [23, 47].

Here, we use scattering-type scanning near-field optical microscopy (s-SNOM) to directly visualize the coupling, hybridization and interference of bonding and anti-bonding modes in the near field of infrared dimer antennas. The excitation of the anti-bonding mode, which is symmetry-forbidden for plane wave illumination, is achieved by rotating the antennas relative to the plane-wave illumination, which introduces retardation and thus symmetry breaking. The excitation of both the bonding and anti-bonding modes allows us to visualize their complex interference directly in the near field of the antennas. We observe a net enhancement or suppression of local fields at specific locations, which can provide a novel strategy for an active control of the near-field enhancement in an optical antenna.

2. Mapping near-field coupling in dimer antennas

Figure 1(a) illustrates the experimental set-up that we use for mapping the near-field distribution and topography of infrared dimer antennas. We use a side-illumination s-SNOM [33, 48, 49] (Neaspec GmbH) where a Si tip, vibrating vertically at frequency Ω , is used to scatter the antenna fields while recording the topography. Using a parabolic mirror objective, the antenna is illuminated at an angle of about 50° from the surface normal with the focused beam of a CO₂ laser ($\lambda_{\text{inc}} = 11.1 \mu\text{m}$), which is polarized parallel to the long axis of the antennas (s-polarization). The same objective is used for collecting the backscattered light. Using a polarizer in front of the detector, we select the horizontally (s-polarized) or vertically (p-polarized) fields backscattered by the tip. Signal demodulation at higher harmonics $n\Omega$ of the tip oscillation frequency in combination with a pseudo-heterodyne interferometric detection [50] yields background-free near-field amplitude $|E_n|$ and phase φ_n maps.

The topography image of a typical dimer antenna studied in this work is shown in Fig. 1(b). It consists of two longitudinally aligned metal nanorods separated by a gap with a nominal width of 50 nm. The antennas were fabricated on a CaF₂ substrate by electron beam lithography and designed to exhibit the fundamental dipolar resonance at a wavelength of about 11 μm . Figure 1(c) shows the s-SNOM amplitude and phase images when the p-polarized backscattered field (yielding mainly the out-of-plane near-field component) is recorded. Note that for better visibility of the antenna phase, we display random phase values by a grey color scale. A random phase occurs in areas where the amplitude signal is below the noise level, which essentially is the case on the substrate where the antenna fields are weak. Each nanorod shows large amplitude signals $|E_{4p}|$ at their extremities that oscillate out of phase for $\varphi_{4p} = 180^\circ$. At the antenna gap no field is observed, owing to the absence of out-of-plane near-field components in the gap center [18]. This near-field amplitude and phase distribution reveals an accumulation of charges of opposite sign at both sides of the gap region [26], which indicates capacitive coupling between the nanorods. Mapping the s-polarized backscattered fields (yielding the in-plane field distribution at the gap), we obtain the amplitude $|E_{4s}|$ and phase φ_{4s} images shown in Fig. 1(d). We observe significant signals at the extremities of the nanorods and an exceptionally intense field $|E_{4s}|$ at the antenna gap. A full width at half maximum (FWHM) of about 50 nm is obtained for this “hot spot”, which agrees well with the nominal gap width (measured by scanning electron microscopy (SEM)). This strongly localized and enhanced field at the gap center further indicates a capacitive coupling between the nanorods and thus, the excitation of a bonding mode in the dimer antenna [45].

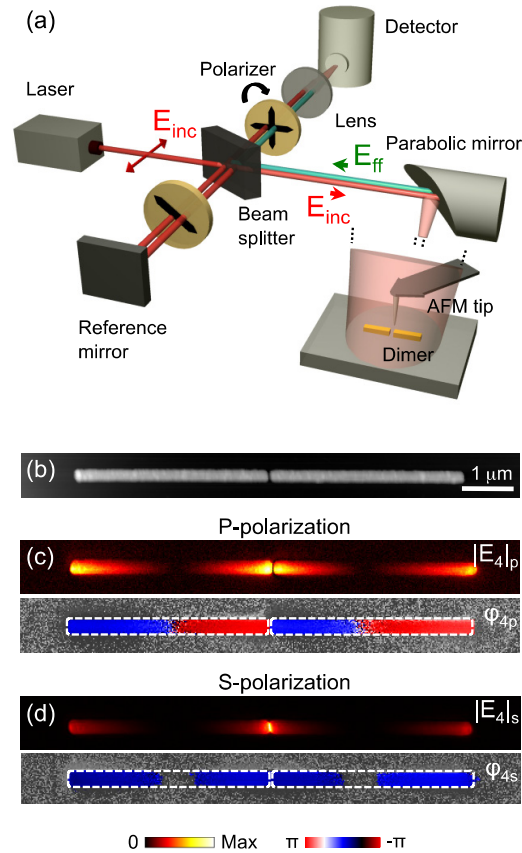


Fig. 1. Experimental set-up and near-field imaging. (a) Illustration of the s-SNOM used for mapping the near-field distribution and topography of infrared dimers. The Si tip, which vibrates at the mechanical resonance frequency Ω of the AFM cantilever, is used to scatter the antenna fields. Using a parabolic mirror objective, the dimer is illuminated with the focused beam of a CO₂ laser (E_{inc}), which is polarized parallel to the long axis of the antennas (s-polarization). The same objective is used to collect the backscattered light (E_{ff}). A polarizer in front of the detector ensures the selection of either s-polarized or p-polarized backscattered fields. Signal demodulation at higher harmonics $n\Omega$ in combination with a pseudo-heterodyne interferometric detection yields background-free near-field amplitude $|E_n|$ and phase ϕ_n maps^[50]. (b) Topography and near-field images of a dimer antenna for (c) p-polarization ($|E_{4p}|$, ϕ_{4p}) and (d) s-polarization ($|E_{4s}|$, ϕ_{4s}) detection schemes. The imaging wavelength is $\lambda_{inc} = 11.1 \mu\text{m}$. The dashed white line in the phase images highlight the nanorods contour.

It is well known that the resonance of the bonding mode of a dimer antenna with gap width g and a total length of $2L + g$ lies at lower energies than the dipolar mode of one single nanorod of length L [15, 16, 32], as illustrated in the schematics of Fig. 2.

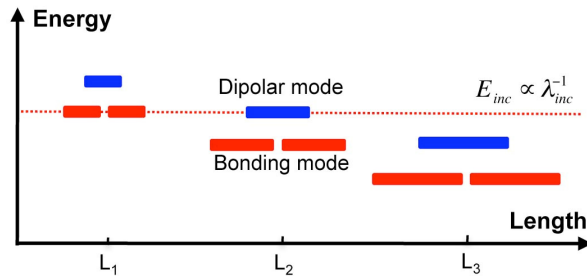


Fig. 2. Diagram of energy levels as a function of nanorod length L for dimer antennas and single nanorods. At a fixed illumination wavelength λ_{inc} (red dashed line) the lower energy bonding mode in a dimer antenna (red) occurs at a shorter nanorod length L_1 than the fundamental.

The measurement of this energy shift would be a clear verification of the capacitive coupling in a dimer structure. In the following we experimentally demonstrate this energy shift in the near field of the antennas. To this end we fabricated sets of dimers and single nanorods of varying length $2L + g$, respectively L , and imaged both of them at $\lambda_{inc} = 11.1 \mu\text{m}$ with our s-SNOM. The gap width g is the same for all dimer antennas. Figure 3(a) shows a schematics of the s-SNOM experiment and Figs. 3(b)-3(d) the topography and near-field amplitude $|E_{4s}|_s$ and phase ϕ_{4s} images of the set of dimer antennas with a nominal gap width $g = 50 \text{ nm}$, obtained by recording the s-polarized backscattered field. The length L of the dimers decreases from the top to the bottom and from the left to the right. Each antenna structure is separated $10 \mu\text{m}$ to the others to avoid any near-field coupling among them.

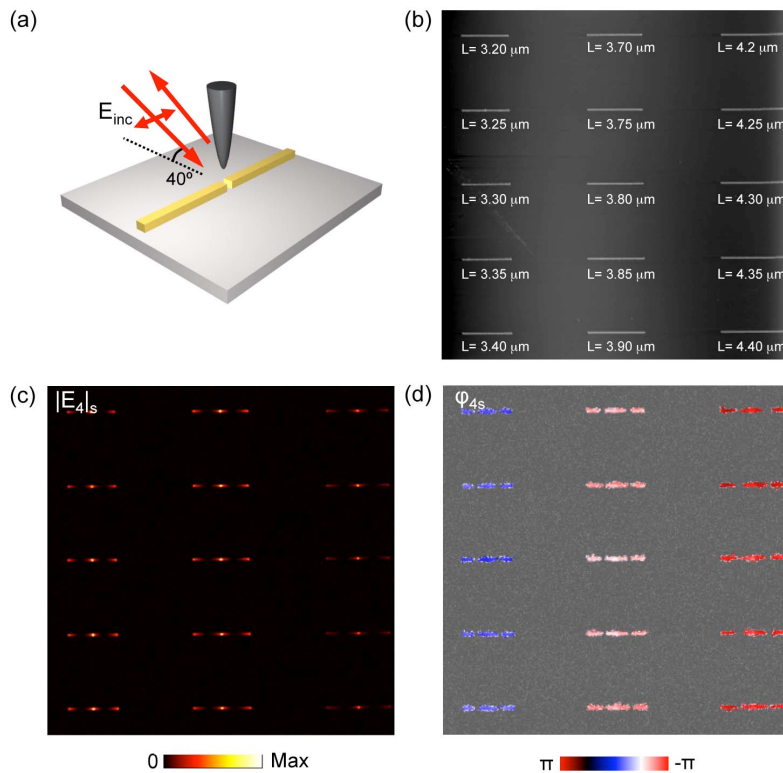


Fig. 3. s-SNOM imaging of dimer antennas. (a) Schematics of the s-SNOM experiment. The longitudinal axis of the antennas is parallel to the incident polarization. (b) Topography, (c) near-field amplitude $|E_{4s}|_s$ and (d) phase ϕ_{4s} images of dimer antennas taken at $\lambda_{inc} = 11.1 \mu\text{m}$.

Figures 4(a) and 4(b) show higher-resolution amplitude $|E_{4s}|$ and phase ϕ_{4s} images of some of the individual antennas. For later comparison with the calculated local field at the antenna, we plot in Fig. 4(c) and 4(d) the square root of the amplitude $\sqrt{E_{4s}}$ and half the phase $\phi_{4s}/2$ measured in the center of the antenna gap (red dots) as a function of nanorod length, since the antenna enhances both the illumination of the tip as well as the scattering from the tip (double scattering process) [49]. We observe that with increasing nanorod length L (from the bottom to the top in Figs. 4(a) and 4(b)) the amplitude signal increases, reaching a maximum at a length of $L_{\text{res-dimer}} = 3.35 \mu\text{m}$. With further increasing length, the amplitude decreases, revealing the resonance behavior of the antennas [51]. The phase (Fig. 4(b), 4(d)) continuously increases with increasing L , which further confirms the existence of an antenna resonance. For comparison we also plot in Fig. 4(c) and 4(d) the square root of the amplitude $\sqrt{E_{4s}}$ and half the phase $\phi_{4s}/2$ measured on top of the extremities of single nanorods (blue dots), as indicated by a blue cross in Fig. 4(d). We note that the single nanorod antennas (images and data published in ref. 49) and the dimer antennas were fabricated on the same CaF_2 substrate within the same e-beam lithography process. All antennas were imaged within one experiment, i.e. with the same tip and the same imaging parameters (same tapping amplitude and demodulation order). We see that the single nanorod resonance occurs at a nanorod length $L_{\text{res-single}} = 3.7 \mu\text{m}$, which is clearly larger than the resonance length $L_{\text{res-dimer}} = 3.35 \mu\text{m}$ of the bonding mode in the dimer antennas. This shift of the resonance length $\Delta L_{\text{res}} = L_{\text{res-dimer}} - L_{\text{res-single}}$ corresponds to a red-shift of the bonding mode, as illustrated in Fig. 2.

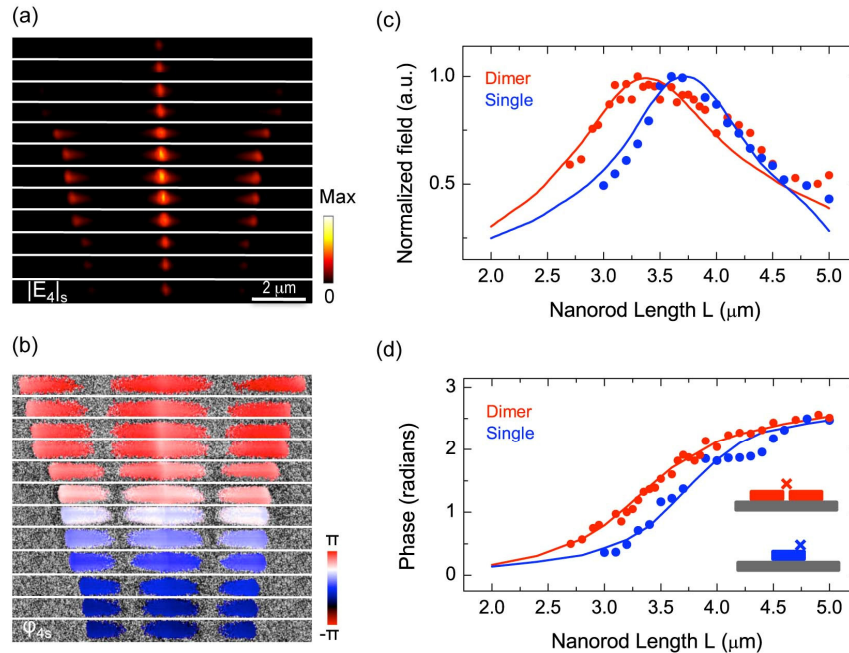


Fig. 4. Verification of near-field coupling in dimer antennas. (a) Near-field amplitude $|E_{4s}|$ and (b) phase ϕ_{4s} images of dimer antennas with a varying length L . The horizontal white lines separate the images taken individually. (c) Comparison of the normalized near-field amplitude $\sqrt{E_{4s}}$ in dimer antennas (red dots) and single nanorods (blue dots) as a function of nanorod length L . (d) Comparison of the near-field phase $\phi_{4s}/2$ in dimer antennas (red dots) and single nanorods (blue dots, data from ref [49].) as a function of nanorod length L . The crosses in the antenna schematics show the locations where the fields were evaluated: the center of the gap for the dimers and the nanorod extremity for the single nanorods. Numerical calculations by FDTD of the in-plane component of the antennas's near-field amplitude and phase are also shown in (c) and (d) by red (dimers) and blue (single nanorods) solid lines.

In order to confirm this result, we calculated numerically by a finite-difference in time-domain (FDTD) method the near-field amplitude and phase (solid lines) at the same antenna locations where the experimental values were measured (marked by crosses in the inset of Fig. 4(d)). We find an excellent agreement between calculations and experiments, corroborating the spectral shift and thus the capacitive coupling in the dimer antennas.

3. Interference of bonding and anti-bonding modes in dimer antennas

The coupling across the gap in the dimer antennas opens the possibility to excite a higher-energy anti-bonding mode, which is characterized by the anti-parallel alignment of electric dipoles at both sides of the gap. The excitation of this mode is symmetry-forbidden for plane waves under normal incidence. It is thus generally referred in the literature to as a “dark” mode. However, it can be excited if the symmetry is broken [22, 23, 29, 52–54]. This can be achieved, as we show in the following, upon rotation of the sample with respect to the incident field, which under a side-illumination geometry introduces a phase shift along the antennas due to retardation.

In Fig. 5 we schematically illustrate the energy splitting into bonding (parallel red arrows) and anti-bonding (anti-parallel blue arrows) modes in dimer antennas for two different nanorod lengths, L_A and L_B .

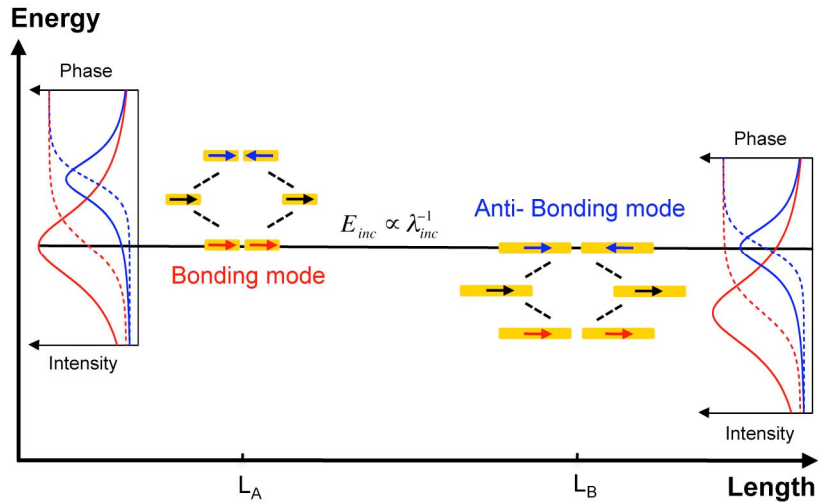


Fig. 5. Diagram of energy levels as a function of nanorod length L for the bonding and anti-bonding modes in dimer antennas. At a fixed illumination wavelength λ_{inc} (black dashed line) the lower energy bonding mode in a dimer antenna (parallel red arrows) occurs at a shorter length L_A than the higher energy anti-bonding mode (anti-parallel blue arrows) at L_B . The graphs display schematic near-field amplitude and phase spectra of the bonding (red) and anti-bonding (blue) modes.

For longer antennas, the energy levels shift to lower energies. Assuming that both modes can be excited, this implies that at a fixed energy/(light frequency) (dashed black line) we can access the bonding mode for short antennas at a nanorod length L_A and the anti-bonding mode when the nanorod length is increased to L_B . Being in resonance with the bonding mode (at length L_A), we expect that this mode dominates the antenna response, as the relatively narrow anti-bonding mode is shifted to significantly higher energies (see schematic spectra to the left). The situation, however, is different when we are in resonance with the anti-bonding mode (at length L_B). Because the resonance of the bonding mode is relatively large (see schematic spectra to the right), it overlaps with the resonance of the anti-bonding mode. Being in resonance with the anti-bonding mode at L_B , we thus expect the excitation and interference of both bonding and anti-bonding modes. In order to study this situation, we imaged dimer

antennas of different length, which were rotated in-plane by 20° degrees in order to break the symmetry and thus to excite both bonding and anti-bonding modes. A sketch of the illumination geometry is depicted in Fig. 6(a) (the p-polarized scattered field is detected, yielding $|E_{3p}|$ and ϕ_{3p} , which corresponds to the out-of-plane local field component).

In Figs. 6(b)-6(d) we show the topography and the experimental near-field amplitude and phase images of the 20° -rotated dimer antennas for nanorod lengths ranging from $L = 2.7 \mu\text{m}$ to $4.8 \mu\text{m}$. The images were taken at $\lambda_{\text{inc}} = 11.1 \mu\text{m}$. For the shortest dimer antenna ($L_A = 2.7 \mu\text{m}$), we observe a symmetric near-field distribution with strong fields oscillating out of phase for 180° at the nanorod extremities and across the gap. This near-field pattern is similar to that obtained for the non-rotated antennas (Fig. 1(c)), indicating that the bonding mode is dominating the optical response of the antenna at this nanorod length (corresponding to the schematics at L_A in Fig. 5).

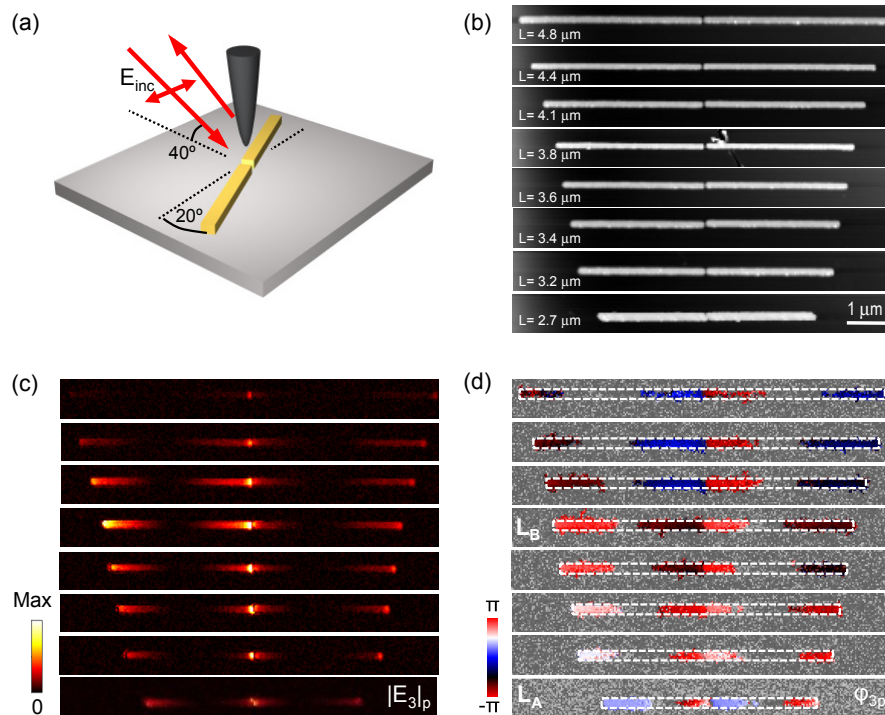


Fig. 6. s-SNOM imaging of 20° -rotated dimer antennas. (a) Schematics of the s-SNOM experiment. The dimer antennas are rotated in-plane by 20° . (b) Topography, and (c) near-field amplitude $|E_{3p}|$ and (d) phase ϕ_{3p} images of dimer antennas with a varying length L ranging from $2.7 \mu\text{m}$ to $4.8 \mu\text{m}$. The horizontal white lines separate the images taken individually.

With increasing nanorod length L (from the bottom to the top in Figs. 6(b)-6(d)), we observe an asymmetry in the near-field distribution. At the extremity of the left nanorod we observe an amplitude maximum at $L_B = 3.8 \mu\text{m}$, while at the extremity of the right nanorod the amplitude is much lower and does not exhibit a clear resonance maximum (Fig. 6(c)). Simultaneously, the phase on the left and right nanorod develops different with increasing nanorod length. On the left side of the gap, the phase increases by about 160° (from red to dark blue in Fig. 6(d)), while on the right side of the gap it increases by about 110° (from light blue to red in Fig. 6(d)). As a result of this behavior, the phase jump across the gap is slightly smaller than 180° for the long antennas, $L > 3.8 \mu\text{m}$ (the change from dark red to light red across the gap corresponds to 120°). We attribute this behavior to the excitation of both bonding and anti-bonding modes in the dimer (corresponding to the schematics at L_B in Fig. 5). Constructive interference on the left nanorod (owing to parallel alignment of the local

dipole oscillations of bonding and anti-bonding modes) yields enhancement of the local fields, while destructive interference on the right nanorod (owing to antiparallel alignment of the local dipole oscillations of the bonding and anti-bonding modes) yields reduction of the local fields.

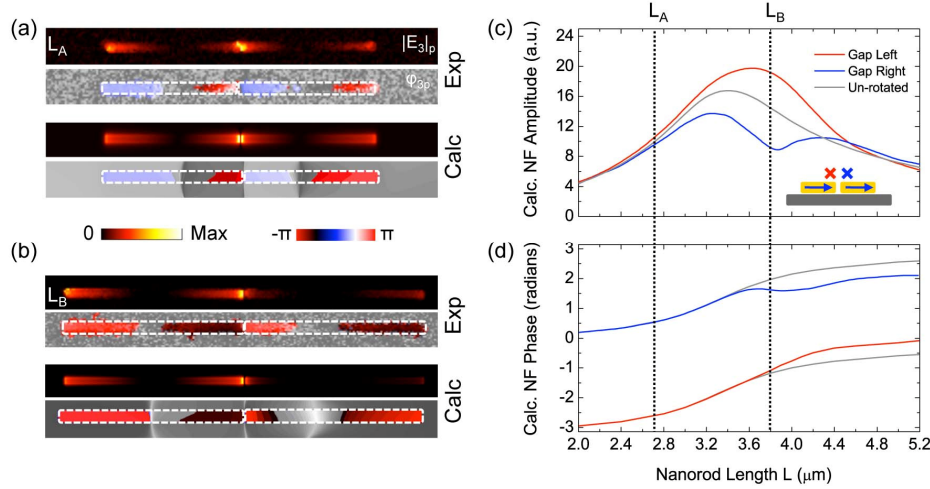


Fig. 7. Interference of modes in rotated dimer antennas. (a) Experimental ($|E_{z|p}$, ϕ_{3p}) and calculated out-of-plane near-field amplitude and phase images for a nanorod length $L_A = 2.7 \mu\text{m}$ and (b) a nanorod length $L_B = 3.8 \mu\text{m}$. (c) Numerically calculated values of the near-field amplitude and (d) phase of the out-of-plane near-field component at the left/right side of the gap (red/blue curve). The red and blue crosses mark the positions at 300 nm from the gap on top of the antennas where the near-field amplitude and phase were extracted from the near-field images. For comparison the near-field amplitude and phase for non-rotated antennas (grey curves) evaluated at the same location are also shown.

To corroborate the constructive and destructive interference of bonding and anti-bonding modes, we performed numerical FDTD calculations of the near-field distribution of the rotated antennas, according to the illumination geometry depicted in Fig. 6(a) (without the tip been considered). In the calculations we apply perfectly matched layers as boundary conditions and assume Gaussian profile for the incident beam. Figures 7(a) and 7(b) show the calculated out-of-plane near-field amplitude and phase images of the antennas with $L_A = 2.7 \mu\text{m}$ and $L_B = 3.8 \mu\text{m}$, exhibiting good agreement with the experimental images (taken from Fig. 6). To understand the asymmetric near-field distribution, we show in Fig. 7(c), 7(d) amplitude and phase values as a function of the nanorod length L , calculated 300 nm to the left and to the right of the antenna gap, and 10 nm above the antenna surface (positions marked by crosses in the inset of Fig. 7(c)). We also show the amplitude and phase for the non-rotated dimer antennas (grey curves) evaluated at the same positions. To quantitatively compare the rotated and non-rotated antennas, we multiplied the amplitude of the latter by the incidence normalization factor $\cos(20^\circ)$. For nanorod lengths around L_B , the amplitude to the left of the gap (red curve) is increased compared to the non-rotated antenna (grey curve), while to the right of the gap (blue curve) the amplitude is reduced and exhibits a dip. This observation substantiates constructive interference between bonding and anti-bonding mode on the left nanorod, and destructive interference on the right nanorod. At lengths below L_A , amplitude and phase on both nanorods match well with that of the non-rotated antenna, as here the anti-bonding mode is negligibly weak (as schematically shown in Fig. 5). At nanorod lengths substantially much larger $L > L_B$, the near-field amplitudes on both sides of the gap become nearly equally strong. However, the phase difference between the left and right side of the gap is significantly reduced to about 120° (see right-hand side of Fig. 7(d)), compared to the non-rotated antennas where the phase jump across the gap is 180° (grey curves). We explain this behavior by a phase shift between the bonding and anti-bonding modes while

both modes exhibit similar field magnitudes (see schematics in Fig. 5) This phase shift between the two modes can be understood by considering that the resonance of the anti-bonding mode is expected for $L > L_B$. Thus, the phase shift between the anti-bonding mode and the incident field (0° reference) assumes values around 90° for $L > L_B$, (right-hand side schematics in Fig. 5), while the phase shift between the bonding mode and the incident field approaches nearly 180° (grey curve in Fig. 7(d)).

4. Summary

In summary, we have presented a detailed s-SNOM study of coupling and hybridization of modes in infrared dimer antennas. In section 2 we verified capacitive near-field coupling and the consequent excitation of the bonding mode. This has been achieved by visualizing the enhanced near-field amplitudes inside the antenna gap and by measuring the red-shift of the resonance in the near-field of the antennas. In section 3 we studied the excitation of the symmetry-forbidden anti-bonding mode in the dimer antennas. To this end, we introduced a rotation of 20° in the antenna illumination geometry, which yields retardation along the antennas and thus a breaking of the system's symmetry. As a result, the excitation of both bonding and anti-bonding modes yields a near-field interference, which manifests in the near-field images as an enhancement and suppression of local fields at specific locations of the dimers. The coupling and interference of antenna modes as shown here provides a useful mechanism for nanoscale coherent control applications.

Acknowledgments

We acknowledge support from the European FP7 projects "Nanoantenna" (FP7-HEALTH-F5-2009-241818-NANOANTENNA), NMP (NMP3-SL-2011-263104- HINTS), and "SPINTROS" (257654), and the National Projects MAT2009-08398, MAT2009-08494 and FIS2010-19609-C02-C01 from the Spanish Ministerio de Ciencia e Innovacion. We also acknowledge the Marie Curie Actions PIRG06-GA-2009-25647, ITAMOSCINOM, as well as the Basque Government Program PI2011-1 and Etorrek-2011 (nanoiker).